Journal of Materials Chemistry C

A General Hierarchical Flower-Shape Cobalt Oxide Spinel Template and Derived Oxide Alloys: Facile Method, Morphology Control and Enhanced Saturation Magnetization

Journal:	*Journal of Materials Chemistry C*
Manuscript ID	TC-ART-08-2020-003762.R1
Article Type:	Paper
Date Submitted by the Author:	15-Sep-2020

Complete List of Authors:	Fu, Zheng; University at Buffalo - The State University of New York, Chemical and Biological Engineering Qiao, Liang ; University at Buffalo, SUNY, Chemical and Biological Engineering Liu, Yang; University at Buffalo - The State University of New York, Chemical and Biological Engineering Xuan, Zhengxi; University at Buffalo (SUNY), Department of Chemical and Biological Engineering Li, Changning; University at Buffalo - The State University of New York, School of Engineering and Applied Sciences Lee, Chaeeon; University at Buffalo (SUNY), Department of Chemical and Biological Engineering Swihart, Mark; University at Buffalo - The State University of New York, Chemical and Biological Engineering

ARTICLE

A General Hierarchical Flower-Shaped Cobalt Oxide Spinel Template: Facile Method, Morphology Control, and Enhanced Saturation Magnetization

Received 00th January 20xx,
Accepted 00th January 20xx

DOI: 10.1039/x0xx00000x

Zheng Fu[a,b], Liang Qiao[a], Yang Liu[a], Zhengxi Xuan[a,b], Changning Li[a], Saranya Rajendra Pillai[a], Chaeeon Lee[a], Mark Swihart[a,b,*]

Nanostructures of materials with the spinel structure and $A_xB_{3-x}O_4$ stoichiometry have been intensively studied due to their many useful magnetic, electronic, and catalytic properties. However, few studies have systematically considered nanostructures of a complete spinel series due lack of stable and general synthesis strategies. This limits the development of rational structure-property-application pathways. Here, we provide a facile and general method to synthesize hierarchical flower-shaped spinel cobalt oxide (SCO) based materials by a one-step solution-phase thermal decomposition. This SCO material serves as an autonomous template to form bimetallic oxide spinels $Fe_xCo_{3-x}O_4$ (Fe-SCO), $Mn_xCo_{3-x}O_4$ (Mn-SCO), $Ni_xCo_{3-x}O_4$ (Ni-SCO), and even the ternary Fe-Ni-Co-O (FNC) spinel in a single step. Morphology control was explored by tuning multiple input parameters such as precursors, ligands, additives, and solvents. The ternary FNC spinel achieved the highest saturation magnetization (98.6 emu/g at 10 kOe) reported for any cobalt spinel. This complete understanding of SCO template with well-controlled shape and magnetization provides a general pathway to flower-like nanostructures of Co-dominant spinels. The SCO templated structures considered in detail here are only tip of the iceberg. We have also produced Cu-, Ag-, Zn-, Pd-, Mo-, Gd-, Pt-, Al-, K-, Li-, and Cr- containing SCO, all showing flower shapes, and combining magnetic properties of Co spinel with properties of the doping elements. We believe this template and approach will be of broad utility for incorporating multiple elements in spinel nanostructures.

1. Introduction

Metal oxides with the AB_2O_4 (or more generally $A_xB_{3-x}O_4$) spinel structure[1] have been widely studied due to their useful electronic,[2-5] electrocatalytic[6-8] and magnetic[9,10] properties and corresponding applications. These AB_2O_4 spinels are constructed from a combination of tetrahedral and octahedral units,[1] in which A and B can be main group metals or transition metals. Numerous studies have investigated synthesis and properties of spinels with Fe, Mn, Co, Ni, Cr, Ga, In and Al occupying the dominant site (B site of AB_2O_4). Spinel metal oxides have been prepared by numerous methods including vapor-phase[11,12] synthesis (e.g., chemical vapor deposition, spray pyrolysis), solution-phase[13-15] synthesis (e.g., sol-gel, hydrothermal) and solid-phase[16,17] synthesis (e.g., thermal decomposition, high-temperature solid-phase methods). However, most reports focus on synthesis and/or applications of one specific spinel material. General methods for controllable synthesis of nanostructures of this class of materials remain lacking. Lack of a comprehensive and systematical synthesis limits the development of rational structure-property-application relationships. In addition, most reports work on the synthesis and properties of ferrite spinels. Few studies were published about $M_xCo_{3-x}O_4$ as a type of cobaltite spinel structure nanomaterials. The cobaltite spinel is a very stable nanostructure with potential applications across multiple fields, such as electrochemistry, magnetic properties, and energy storage. Here, we present an integrated systematic approach to the design and synthesis of cobalt-dominant spinel materials. We use a one-step solution phase synthesis method to produce three-dimensional (3D) hierarchical flower-shaped cobalt oxide spinel (Co_3O_4) nanocrystals (NCs) with curved one-dimensional (1D) flexible arms. This structure serves as general structural template to produce other $M_xCo_{3-x}O_4$ spinels (M = metal elements) with the same flower-like morphology. Unlike most template methods,[6] these spinel cobalt oxides (SCO) readily incorporate other metals, while maintaining both the spinel crystal structure and branched flower morphology, in a simple one-pot heating method. Therefore, we have applied this template to many metals in a one-step solution phase synthesis, mixing all chemicals in one flask, and adjusting additives and ligands to achieve shape control. The successful synthesis of Co-, Fe-, Mn-, Ni-, Cu-, Ag-, Zn-, Pd-, Mo-, Gd-, Pt-, Al-, K-, Li-, Cr-containing spinel SCO with this autonomous template approach demonstrates its stability and extensibility. In addition, the 3D hierarchical flower shape exhibits higher specific surface area than compact structures, and this surface area is more accessible than in porous structures. Both of these factors are valuable in potential catalytic applications. Composed of many small spherical dots, the 3D flower is more flexible than other traditional flower shapes. This also makes it easier to control the

[a] Department of Chemical and Biological Engineering, University at Buffalo (SUNY), Buffalo, New York 14260, United States.
[b] RENEW Institute, University at Buffalo (SUNY), Buffalo, New York 14260, United States. E-mail: swihart@buffalo.edu (MTS)

Electronic Supplementary Information (ESI) available: [details of any supplementary information available should be included here]. See DOI: 10.1039/x0xx00000x

magnetic domains which correspond to each single spherical spinel dot.

Synthesis of binary or ternary transition metal spinel oxide nanomaterials usually requires more than one step, as in seed-mediated growth[18] or hot injection methods.[19] Such methods, which depend upon rapid mixing, can be difficult to reproduce and to scale to larger sizes for practical application. The approach presented here, in which we combine all the chemicals and then react them in one slow heating step is enabled by the stable SCO autonomous template. This highly reduces the total reaction time while improving reproducibility and scalability. Moreover, such a stable autonomous template for multi-metal nanomaterials may be more broadly applicable as a new synthesis approach for application in future research.

Sun and co-workers synthesized uniform nanoparticles of MFe_2O_4 and $M_xFe_{3-x}O_4$ to improve coercivity[20] and performance in electrocatalysis of the oxygen reduction reaction (ORR).[8] Herein, we mainly consider the effect of composition and morphology of $M_xCo_{3-x}O_4$ NCs on their saturation magnetization. We present detailed results for M = Fe, Ni, and Mn, exploring the effect of synthesis conditions on morphology, and the effect of M on magnetization behavior. The Fe-Ni-Co-O tri-metallic spinel prepared here achieved the highest saturation magnetization reported for spinel metal oxides.

2. Results and Discussion

2.1. Shape-controlled synthesis of SCO template and derived alloys.

With the development of *in situ* TEM, some nanoparticle growth processes can be observed directly. However, for many materials, including those larger than the typical dimensions of *in situ* TEM cells, this is not feasible, and relating *in situ* TEM results to practical synthesis methods remains challenging. Thus, to deeply explore the shape and size evolution of SCO-based NCs and elucidate the effects of input parameters such as precursor concentrations, ligands, additives, heating rate, and reaction time, we have employed conventional synthesis followed by *ex situ* TEM analysis. The resulting TEM atlas of shape evolution (Figure 1) helps to build comprehensive understanding of morphology control of M-SCO nanomaterials. Three transition metals with properties similar to cobalt, specifically Fe, Mn, and Ni, were selected for this systematic analysis. The four quadrants of the TEM atlas in Figure 1 correspond to the SCO template (Co_3O_4, blue frames) and derived Fe-SCO ($Fe_xCo_{3-x}O_4$, red frames), Mn-SCO ($Mn_xCo_{3-x}O_4$, yellow frames) and Ni-SCO ($Ni_xCo_{3-x}O_4$, green frames). The colors correspond to the colors of the precursors dissolved in ethanol. As discussed further below, the combination of TOP, OA, and OAm is crucial for promoting the growth of flower-like structures with one-dimensional arms. Unless otherwise specified, these three additives were employed together in all experiments as other factors (solvent, ligand, precursors, etc.) were varied.

2.1.1. SCO template. The hierarchical flower-shaped SCO template (Figure 1, panel A11) is prepared by a facile one-step hot colloidal synthesis that simply requires controlled heating of the precursor mixture. To explore the stability and extensibility of this template, different transition metal precursors were tested as indicated by arrows ⑫, ⑬, and ⑭, which correspond to addition of Fe, Mn, and Ni, respectively. The M:Co precursor ratio for each of these cases was 0.5:1, corresponding to the ideal AB_2O_4 stoichiometry. Sample B8 (Fe-SCO), C2 (Mn-SCO) and D2 (Ni-SCO) were obtained using the same conditions employed for the SCO template (A11).

Elemental analysis of these samples by energy dispersive X-ray spectroscopy (EDS) showed that the Fe, Mn, or Ni to Co ratio in the product particles was lower than the 0.5:1 ratio of the precursors. Therefore, Fe-SCO, Mn-SCO, and Ni-SCO here represent $Fe_xCo_{3-x}O_4$, $Mn_xCo_{3-x}O_4$ and $Ni_xCo_{3-x}O_4$, respectively. Varying the A:B ratio to produce $A_xB_{3-x}O_4$ with different *x* values also altered the size and shape of the nanostructures. All of these compositions share the spinel crystal structure and similar hierarchical flower shape with long arms. However, producing pure Fe, Mn, and Ni oxides, shown as samples B1, C1 and D1, respectively, yielded spherical or quasi-spherical particles. These samples were produced only using Fe, Mn, or Ni, without introducing cobalt, indicating that the SCO template plays an essential role in guiding the growth of flower-like spinel structure nanoparticles.

2.1.2. Ligand effects. Ligands adsorbed on the growing nanoparticle surfaces play a crucial role in determining the size and morphology of the nanostructures produced here. We tested several ligands for their ability to guide the growth of flower-like structures in the SCO system. Dodecylamine (DDA), dodecanediol (DDD), tetradecanediol (TDD), oleylamine (OAm), oleic acid (OA), and trioctylphosphine (TOP) can all coordinate with transition metal ions. In this study, we classify OAm, OA, and TOP as additives, rather than ligands, due to the low concentrations of these substances considered. They are discussed in a separate section below.

For the SCO template, three common ligands DDA, DDD, and TDD were studied to ensure a stable and extensible template. Samples shown in panels A5, A8, and A11 of Figure 1 were obtained using TDD, DDD and DDA, respectively (connected by arrows ③ and ④). All three ligands produce particles showing hierarchical flower shapes. However, those prepared with DDD and DDA show one-dimensional long arms, while those synthesized using TDD show two-dimensional petals growing out of a central core. Upon increasing the heating rate (arrows ⑦ and ⑨), particles prepared using TDD (A5 to A3) do not maintain their hierarchical shape, but those prepared using DDD retain their flower-like structure with 1-D arms. A previous study of bidentate diol ligands showed that the diol with shorter chain length more strongly limited growth of Fe_3O_4.[21] This is consistent with the observation here that DDD is better able to guide the growth of SCO structures compared with TDD.

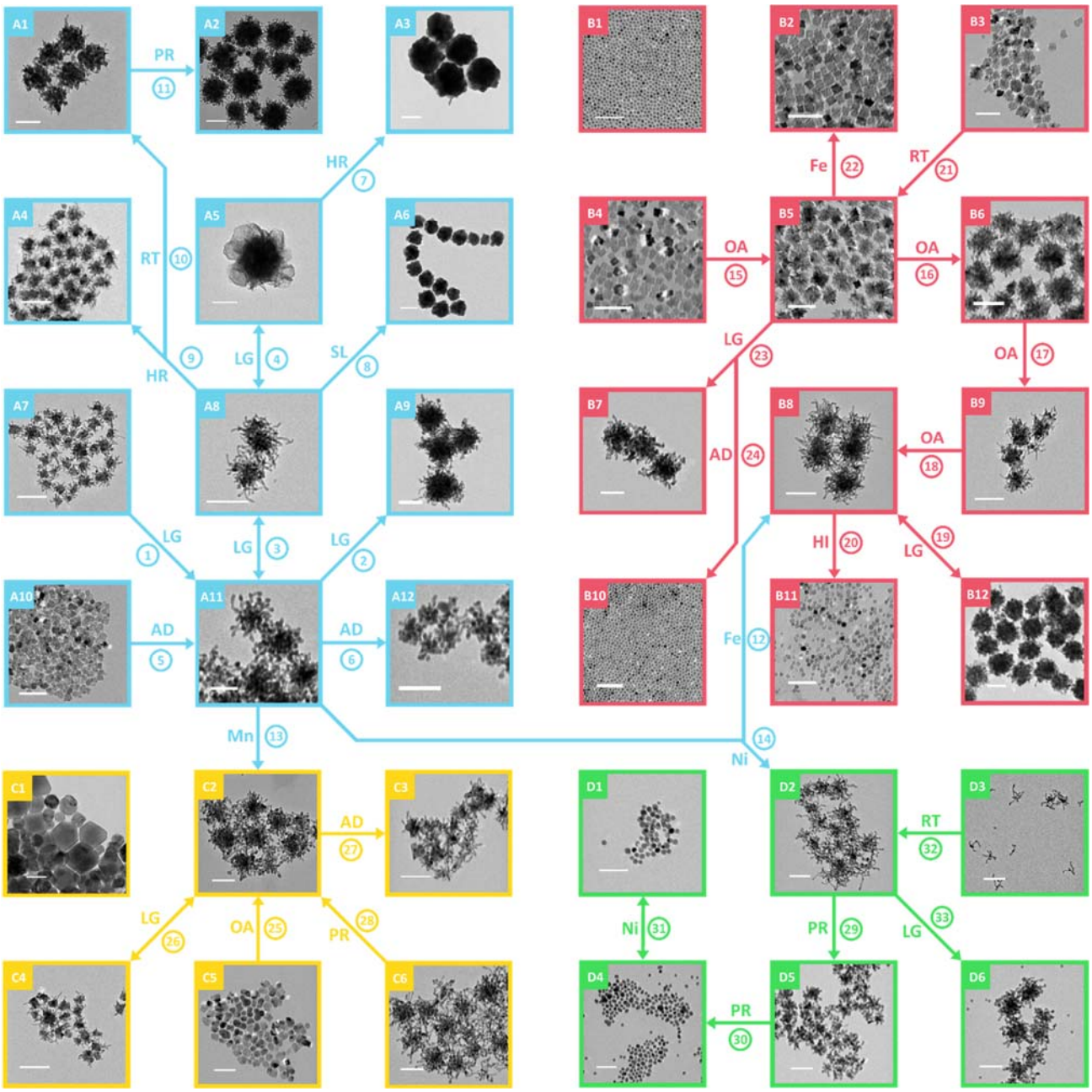

Fig. 1 TEM atlas of SCO template (blue frames), Fe-SCO (red frames), Mn-SCO (yellow frames) and Ni-SCO (green frames). Single-headed arrows represent an increase or decrease in a parameter (e.g., concentration or temperature), and double-headed arrows represent replacement of one substance with another. Abbreviations labeled on arrows are PR for precursor, HR for heating ramp rate, RT for reaction time, LG for ligand, SL for solvents, AD for additive, OA for oleic acid and HI for hot injection. Scale bars are 100 nm.

The above observations led us to focus on the 12-carbon ligands, DDD and DDA, for further exploration. The distinction between these two ligands is their terminal group, a diol or amine. Fe-SCO and Mn-SCO particles with DDD (B12 and C4) had larger or smaller size and shorter arms than those prepared with DDA (B8 and C2), which showed a more uniform hierarchical flower shape (arrow ⑲ and ㉖, Figure 1). Overall, the ligand with a reductive amine terminal functional group, DDA, proved more effective across all compositions to promote growth of hierarchical flower-like SCO structures compared with DDD and TDD.

Ligand concentration is commonly used to tune particle size in hot colloidal synthesis. Increasing DDA ligand concentration (arrows ①, ②, ㉓, and ㉝) increases the average size of all types of SCO, while shortening the 1D arms. This trend runs counter to the intuitive expectation of a ligand limiting growth, such that higher ligand concentration would be expected to produce smaller particles. We observe that DDA first promotes the growth of arms (arrow ①), but beyond a critical concentration, further addition of DDA promotes the growth of cores more than the growth of arms, yielding larger particles with shorter arms (arrow ②, ㉓ and ㉝). This effect presumably arises from the multiple roles that DDA plays in controlling the initial particle nucleation, the growth of primary particles, and the assembly of primary particles into hierarchical flower-like structures. Thus, ligand concentration mostly affects the overall particle size but also has some effect on the particle morphology.

2.1.3. Additive effects. Many studies have explored the synergies among additives such as TOP, OAm, and OA in growth of metal oxide nanostructures.[22-24] Here, we employ small changes in additive concentrations, in the presence of a primary ligand, to control the growth of hierarchical flower-like SCO nanostructures.

Samples prepared without TOP (A10, B10) are spherical or quasi-spherical, without the flower-like hierarchical structure, demonstrating the decisive role of TOP in triggering the assembly process that produces these structures. However, further increasing the amount of TOP (arrows ⑥ and ㉗) reduces particle size by both shortening the arms and decreasing the core size, as observed in other reports.[25,26] Thus, TOP is an essential additive to produce M-SCO with a hierarchical flower shape and to maintain particle size.

Oleylamine (OAm) and oleic acid (OA) play cooperative roles in guiding nanostructure growth. OAm appears to play a lesser role in this case. Although OAm is essential for producing the hierarchical flower-like structures, varying its concentration had minor effects on particle size or shape. In contrast, a sufficiently high concentration of OA will suppress the formation of one-dimensional arms (arrow ㉕), especially in the case of Fe-SCO (arrows ⑱, ⑰, ⑯, ⑮, each representing a decrease in OA concentration). The growth mechanism of Fe-SCO appears to differ from that of the other compositions considered here. Upon decreasing the OA concentration successively, Fe-SCO cube-stars (B4) grow 111-faceted spikes from their corners and begin to assemble to form larger cubes (B5) with extremely extended corners (B6) via diffusion growth. However, excessive reduction of OA concentration reduced the incorporation of Fe in $Fe_xCo_{3-x}O_4$, resulting in the aggregative growth observed for other M-SCOs to form long-arm flowers (B9 and B8). The detailed growth mechanism (Figure 2) including both diffusion and aggregation processes, is discussed further below. Overall, OA here is a crucial additive to adjust morphology and trigger different growth mechanisms.

2.1.4. Precursor effects. The images in the top left position (B1, C1, and D1) for each material (Fe-SCO, Mn-SCO and Ni-SCO, respectively) show particles of pure Fe-O, Mn-O and Ni-O, respectively, prepared by the same protocol but without any Co precursor. Without Co, these each form dense crystalline particles without the hierarchical structure observed when Co is present. For the hierarchical mixed SCO structures, increasing the quantity of Fe, Mn, or Ni precursor narrows the particle size distribution and shortens the arms (arrow ㉒, ㉘, ㉙, and ㉚). This demonstrates that increased concentration of other metal precursors weakens the SCO templating effect. For example, from sample D2 to D5 to D4 (arrow ㉙ to ㉚), the ratio of Ni:Co in Ni-Co-O material was increased by adding nickel precursor. Both particle size and arm length shrunk, tending toward the shape of pure Ni-O (D1, arrow ㉛). In the same way, more iron precursors convert the Fe-SCO particles to uniform monodisperse cubes (arrow ㉒), whose growth is similar to that of iron oxide nanocubes.[21] As one might intuitively expect, the concentration of precursors influences the dominant element in the final product.

2.1.5. Duration. Varying reaction time provides a means to explore the growth process. A critical time point in the growth of flower-shaped particles occurs when formation of long arms is complete, and individual small particles are rare. Before this point, the small dots aggregate to form cores and arms that make up the flowerlike structure (e.g. arrow ㉜). For the particles that have already passed this point, like A8, extending reaction time further (arrow ⑩) yields larger particle size and denser structure via further core growth. This is similar to the effects of increasing ligand concentration (arrow ㉝) or precursor concentration (arrow ⑪). Moreover, examining products at short reaction time (panel D3) also provides insight into the growth mechanism. Here, 20 min shorter reaction time yields small spherical dots and immature flowers with scattered arms. At this point, the dimensions of the small particles and arms are similar to those in the final fully-grown flower-like structures (panel D2). This suggests that from 70 min (panel D3) to 90 min (panel D2) reaction time, growth of hierarchical structures primarily occurs by aggregation of these smaller structures and not by growth of the smaller structures themselves.

2.1.6. Heating ramp. Increasing heating rate accelerates the decomposition of precursors and causes particle nucleation to occur at a shorter reaction time. Because particle nucleation and growth are more strongly temperature dependent than particle aggregation, this can favor growth of cores over aggregation to produce flower-like structures. This was observed across experiments using different ligands, though the details of the effects were varied. Particles may have larger cores with shorter arms (A4, arrow ⑨), or finish their growth without forming branched hierarchical structures (A3, arrow ⑦).

2.1.7. Method. Hot injection is often used to prepare particles with a narrow size distribution by inducing a rapid burst of nucleation followed by a separate period of growth by reaction of nuclei with atomic or molecular precursors. Applying hot injection rather than one-pot heating (arrow ⑳) to synthesize

Fe-SCO leads to formation of dense and relatively monodisperse particles (B11) rather than formation of flower-like SCO structures. Compared to hot injection, the one-step solution phase method simplifies the synthesis and allows a stable and magnetic hierarchical branched SCO template to grow in this system. Importantly, one-pot heating methods are generally more scalable than hot injection methods, because they are less sensitive to mixing rates, which vary greatly with reaction scale.

2.1.8. Morphology control summary. From above discussion, we learned that this syntheses provides a stable system to produce $M_xCo_{3-x}O_4$ flower-like nanoparticles. DDA, DDD, and TDD as ligands all lead to the 3-D flower shape. However, the different lengths of these carbon chain ligands and their concentration may affect the flower size. This effect can be rationalized in the context of the LaMer nucleation theory. TOP, OAm, and OA used as additives here influence the formation of the flower shape, although they are used in much smaller quantities compared with ligands and solvents. Although OAm is essential for producing the flower structure, varying its concentration has relatively minor effects on both particle size and shape. In contrast, decreasing the concentration of OA triggers a transition from cube-star FeO/CoO to flower-like $Fe_xCo_{3-x}O_4$. Reaction time and heating rate effects are consistent with classic nucleation theory,[27] in that longer reaction time and higher temperature produce larger core sizes via aggregative growth.

2.2. Composition analysis

Representative SCO samples were characterized by XRD, TEM, and XPS, as shown in Figure 2. XPS spectra in the Co 2p, Fe 2p, Mn 2p, and Ni 2p energy ranges provide information on the oxidation states of elements in each phase corresponding to the XRD patterns. Larger and clearer versions of XPS spectra of the samples in Figure 2 are provided in Figure S5 (SI). XRD patterns in Figure 2(a), (b), (c) and (d), for flower-like M-SCOs, each show the $A_xB_{3-x}O_4$ spinel structure. The main peaks of each pattern match the lattice spacings observed by HRTEM. Among these, sample (c) Mn-SCO shows evidence of the spinel structure, but mainly shows peaks corresponding to CoO, with clear peaks matching the CoO 111 and 200 reflections, and weak peaks of $MnCo_2O_4$ spinel. Also, the hysteresis loop of Mn-SCO (Figure 4) showed the lowest saturation compared to other M-SCOs, consistent with the presence of a substantial fraction of CoO. Both XRD and hysteresis curves demonstrate that Mn-SCO is a mixture of CoO and $Mn_xCo_{3-x}O_4$. As evident in Table S3, Mn is incorporated at a lower concentration than the other cations, indicating a low Mn occupancy of A sites. This is accompanied by formation of CoO, with all Co in the 2+ oxidation state, which also lowers the saturation magnetization. This provides valuable guidance on design to enhance magnetic properties of M-SCOs. Compared to flower-like samples (a), (b), (c), and (d), sample (e) shows clear differences in both morphology and XRD pattern (Figure 2). Fe-SCO synthesis with increasing concentration of OA (arrows ⑱, ⑰, ⑯, and ⑮, Figure 1), produces distinct morphologies and compositions, demonstrating a different growth process compared to the other SCO samples. In terms of morphology, flower-shaped SCO samples like (a) - (d), are composed of many small spherical particles (Figure 3(a) and (f) to (g)). On the other hand, sample (e) shows an assembly of numerous cube stars, whose corners are extended, exposing 111 facets. Sample (e), composed of FeO and CoO, shows essentially zero saturation magnetization, demonstrating that varying the concentration of OA alters morphology, composition, crystal structure, and corresponding properties.

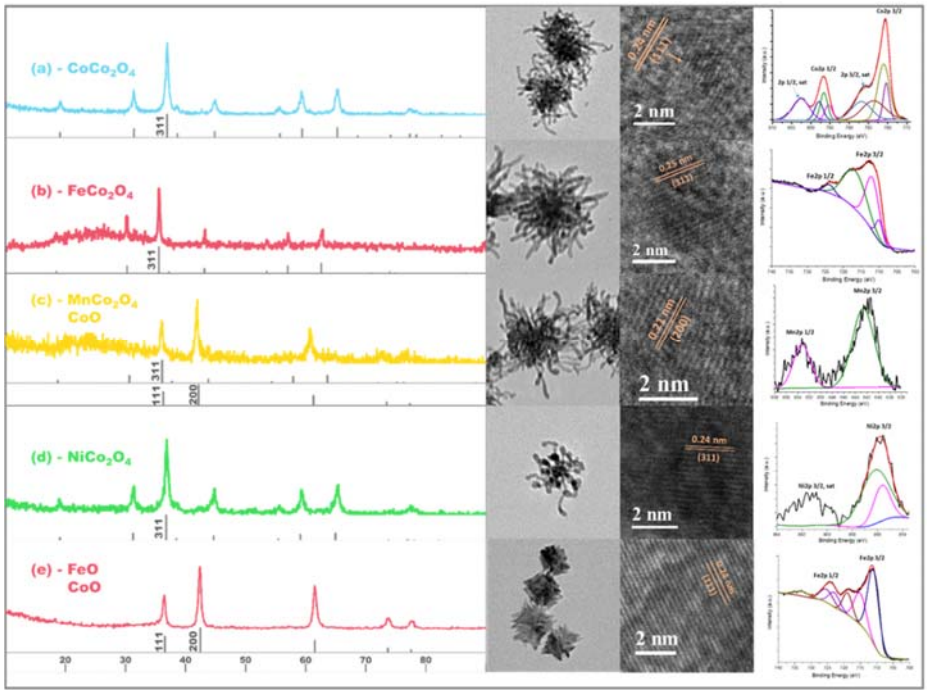

Fig. 2 XRD patterns, TEM and HRTEM images, and XPS spectra of M-SCO samples: (a) Co3O4 template, (b) Fe-SCO, (c) Mn-SCO, (d) Ni-SCO, (e) FeO/CoO samples.

ARTICLE

In addition, observing the composition of Mn-SCO shows that changing the A-site element can affect the crystal phase in the final products, which reduces both the saturation magnetization and coercivity (Figure 4). In both cases, final crystal phases are determined by composition and, in turn, set the saturation magnetization. Thus, we tune the morphology and adjust magnetic properties via controlling the composition of samples.

2.3. Proposed growth mechanisms

Given the TEM atlas, XRD and HRTEM images, we propose the growth mechanisms presented in Figure 3. Figure 3b shows precursors of Co, Fe, Mn, and Ni dissolved in toluene, with four different colors: blue for Co, red for Fe, yellow for Mn and green for Ni as used throughout the paper to represent these elements. Figure 3c, d, f, and g show corresponding TEM images illustrating morphology evolution during growth (Figure 3a). Figure 3e illustrates the crystal structure of Co_3O_4, with blue spheres for Co and red spheres for O. Among the cobaltite spinel materials studied here, the $A_xB_{3-x}O_4$ spinels have this same structure, with 2+ ions occupying tetrahedral sites and 3+ ions in the octahedral sites. Because these materials do not follow the ideal AB_2O_4 stoichiometry, a given element (e.g., Fe or Co) may be present in multiple oxidation states and occupy both cation sites.[28] Due to the unique growth of Fe-SCO, we separate it into its own path (Figure 3a) as indicated by the red arrow for Fe-SCO and blue arrow for Co-, Mn-, and Ni-SCO growth mechanisms. In addition, the blue arrow path applies to many other elements from which M-SCO nanostructures have been produced, illustrating the stability and generality of the hierarchical flower-like SCO template approach.

As described in more detail in the experimental section, all of the branched flower-like structures were produced by a one-step synthesis method. Although a SCO template governs the morphology of the Fe-, Mn- and Ni-SCO nanostructures, we do not prepare this template separately. As illustrated in Figure 3a, all the precursors, ligands, additives and solvents are mixed together before heating to the synthesis temperature. In the growth pathways for both Fe-SCO and other M-SCO materials, the first two steps are those of classic nucleation and growth theory.[29] Initially, precursor ions or complexes react to form monomers. Nucleation occurs when the monomer concentration sufficiently exceeds its saturation concentration. HRTEM Figure 3f shows part of an arm of a representative flower-shaped NC, demonstrating that it is composed of numerous small quasi-spherical dots with random orientation surrounded by a SCO template frame protection. The small crystallite size is also reflected in the weak, broadened peaks

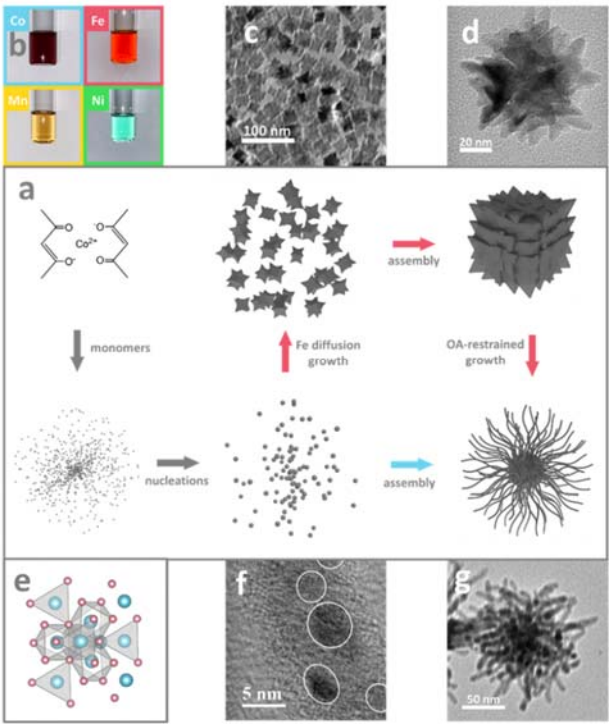

Fig. 3 A possible growth mechanism of the SCO template and Fe-, Mn-, Ni-SCO nanostructures. (a) Schematic illustration of proposed growth pathways, (b) photograph of precursor solutions, (c) Fe-SCO cube-star structures, (d) Fe-SCO nanostructures with extended corners, (e) spinel crystal structure (blue = M, red = O), (f) HRTEM image of a single arm of Fe-SCO structure, and (g) representative Fe-SCO produced with high OA concentration, exhibiting branched flower-like morphology of the SCO template.

observed in XRD. This suggests that aggregation of small primary particles (nuclei) is the next stage of growth. These small particles presumably each act as a single magnetic domain, as discussed further below. Next, the growth pathway bifurcates, as indicated by the red and blue arrows, respectively, in Figure 3.

For most of the M-SCO materials (blue arrow), the heteroatom (M element) combines with cobalt to form monomers and to nucleate the small dots assembled by agglomerative growth[30] to form a hierarchical flower shape. From TEM images of products from different reaction times (Figure 1 B3), we see that shorter reaction time produced smaller, less branched particles accompanied by small dots (Figure 1 D3, reaction time of 70 min) among the growing blossoms, suggesting that flower-like

particles are composed of these small dots and are not yet fully assembled after 70 min. Table S3 compares the M:Co (M= Fe, Mn, Ni) atomic ratios measured by EDS and XPS for the representative samples in Figure 2. In each case, the M:Co ratio from XPS is much lower than that measured by EDS, suggesting that the M element in the M-SCO is mainly present in the core part, where it is detected by EDS but is beyond the sampling depth of XPS. This observation is consistent with our observations for Cu-SCO and Ag-SCO that we are investigating in a follow-up study, in which the core contains only Ag and/or Cu.

Fe-SCO growth appears to follow a different pathway (red arrow) in which Fe atoms continue to deposit on growing nuclei, in a facet-dependent manner. The initial small dots grow in a facet-specific diffusion-controlled[31] manner to form cube stars via passivation of (100) facets to form cubes followed by continued deposition at the corners of the cubes. Later, after the precursor is consumed, these can aggregate into larger particles that retain the cube-star structure. This preferential growth on 111 facets has also been observed on other nanocubes or stars of metal oxides.[9,32,33] When the concentration of oleic acid is reduced (Figure 3d to g), nucleation appears to be faster and consumes the Fe precursors before they grow into cube stars. In this case, $FeCo_2O_4$ grows into a flower shape similar to the other M-SCO materials. Other researchers [34,35] also observed similar behavior in which OA plays a key role in controlling particle size among spinel-structured materials. In those studies, as observed here, nucleation and aggregation of primary particles are inhibited and growth and faceting are promoted with increasing OA concentration. Thus, growth into cubes and cube stars is favored over aggregation of the initial small dots. Here, we already know the Fe-SCO cube stars (Figure 3c) and M-SCO (Figure 3g) both grow from small spherical dots. The difference between them is that for Fe-SCO prepared at higher OA concentration, slow deposition of Fe atoms continues after nucleation, preferentially growing 111 facets to produce cubes and then cube stars, as also observed in our previous research on Fe_3O_4.[21] The relatively sharp peaks in CoO/FeO XRD patterns and 111 planes visible in the HRTEM in Figure 2e demonstrate the greater crystallinity and larger crystallite size in these nanostructures compared to the other flower-like structures.

More broadly, increasing OA concentration not only promotes growth on 111 facets in Fe-SCO synthesis, but also favors deposition of metal atoms onto initial nuclei, rather than rapid nucleation followed by aggregation into flower structures, for the other M-SCO materials. Other M-SCO materials do not exhibit facet-selective growth to form cube stars like Fe-SCO, but simply produce larger quasi-spherical nanoparticles as shown in Figure 1 C5. Following the Fe-SCO path (red arrow), cube star growth and assembly occurs at relatively high OA concentration (Figure 3d, 0.475 mol/L). In contrast, lower OA concentration (0.158 mol/L) leads to growth of flower shaped aggregates (Figure 3g) composed of small spherical dots. Higher OA concentration also allows higher levels of incorporation of M in each M-SCO material. The atomic ratio of Co: Fe is around 1:1 in cube stars (Figure 3c), yet around 1:0.5 in flower shaped nanostructures (Figure 3g). The situation is similar for other M-SCO nanostructures, with both the degree of branching or blossoming and the M content depending upon the OA concentration. For both Fe-SCO and M-SCO paths, reducing OA concentration (to 0.158 mol/L) will produce 3-D hierarchical flower shapes. However, we cannot obtain this SCO flower shape template with zero OA concentration (Figure S2) due to the coordination among each ligand and additive. Thus, OA plays an essential role in controlling the morphology of M-SCO.

2.4. Magnetic properties

We characterized the magnetization behavior of four prototypical M-SCO materials: the SCO template, Fe-SCO, Mn-SCO, and Ni-SCO with hierarchical flower shapes. From Figure 4, we see that the coercivity of these spinel nanostructures was around 283 Oe for Co_3O_4, 420 Oe for $Fe_xCo_{3-x}O_4$, 214 Oe for $Mn_xCo_{3-x}O_4$, and 196 Oe for $Ni_xCo_{3-x}O_4$. The Co_3O_4 SCO template (blue curve) shows a common spinel saturation magnetization, around 46.0 emu/g. Ni-SCO (green curve) exhibits slightly higher magnetization (50.0 emu/g) while the saturation magnetization of Fe-SCO (red curve) was lower (around 22 emu/g). Using the flower-like SCO template to make Fe-SCO and Ni-SCO affects their saturation magnetization, but the resulting values are still in a range typical of M-SCO materials. In contrast, Mn-SCO (yellow curve) shows an abnormally low saturation magnetization of around 3.7 emu/g. The XRD pattern of Mn-SCO in Figure 2 suggests that the Mn-SCO sample contains non-magnetic CoO, which reduced the saturation magnetization of Mn-SCO. Addition of Mn appears to promote growth of a CoO-dominant $CoO/Mn_xCo_{3-x}O_4$ mixture rather than uniform incorporation of Mn into $Mn_xCo_{3-x}O_4$.

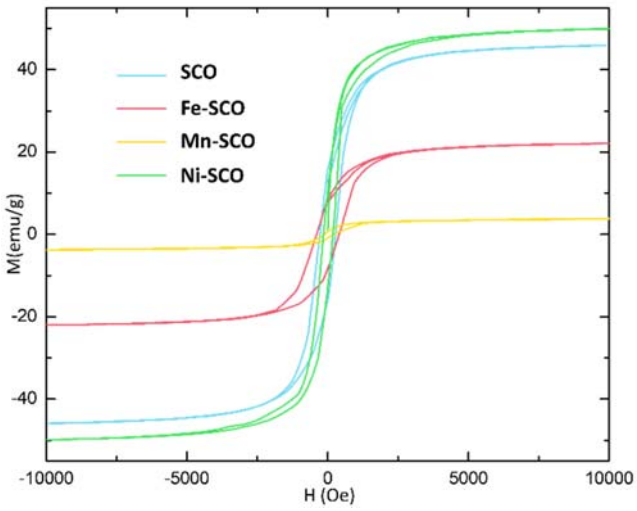

Fig. 4 Hysteresis loops of SCO template (blue curve), Fe-SCO (red curve), Mn-SCO (yellow curve) and Ni-SCO (green curve).

Following the above characterization, we tuned the composition ratio to enhance the magnetic properties of this spinel. Here, Fe doping increased the coercivity, while Ni doping increased the saturation magnetization. Thus, we prepared a

trimetallic (ternary) Fe-Ni-Co-O (FNC) spinel, using SCO as the hierarchical template, simultaneously, to potentially increase both coercivity and saturation.

This FNC spinel shows a similar hierarchical flower shape to the SCO template. Two representative FNC spinel samples are chosen due to the following reasons. Higher Co ratio allows the stable flower-like SCO template as spinel structure. Doped Ni in this cobaltite spinel plays a significant role on enhancing the saturation magnetization. However, from Fig. 1 we learned that high ratio of Ni leads to spherical shape. Thus, a ratio of Ni:Co=0.1 and 0.05 is chosen to not only enhance the M_s but also maintain the 3D flower shape. By tuning the ratio of Fe, Ni and Co, FNC spinel (a) (1:0.3:0.1 Co:Fe:Ni ratio in precursors, blue curves and frames in Figure 5) was smaller in size than FNC spinel (b) (1:0.5:0.05 Co:Fe:Ni ratio in precursors, red curves and frames). FNC spinel (a) shows a similar coercivity with M-SCO around 380 Oe, but shows a high saturation magnetization of 98.6 emu/g at 10k Oe, and the larger size FNC spinel (b) reached 88.5 emu/g at 10k Oe. These values are higher than commercial magnetite fine powder, with a saturation magnetization of 84.5 emu/g, and higher than other common spinels reported in the literature.

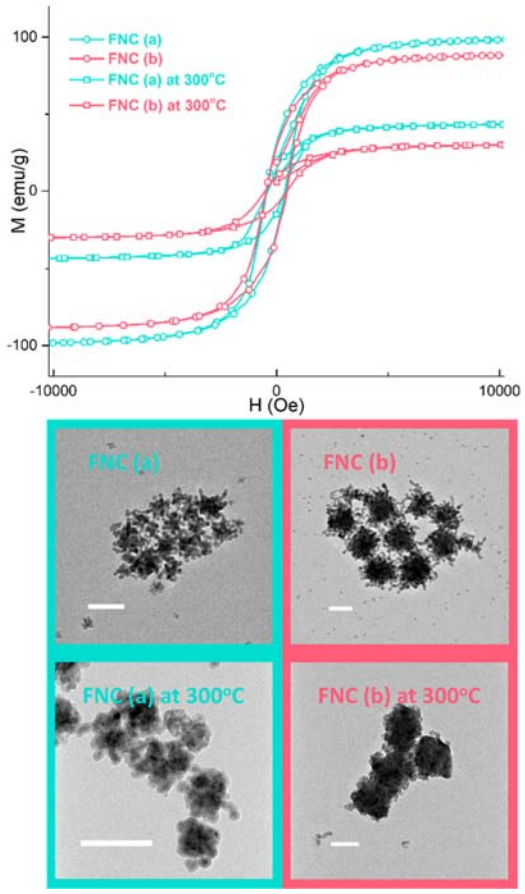

Fig. 5 Hysteresis loops and TEM images of ternary FNC spinel (a) and (b), and their annealed samples. Scale bars are 100 nm.

Among those samples composed of numerous small spherical dots, two factors affect the saturation magnetization: the composition and the ordering of magnetic dipoles. M_s is mostly determined by the composition and crystal structure of materials. Magnetic ordering arises from superexchange interactions among the metal ions in the spinel structure.[36] From FNC (a) to (b) shown in Fig. 5, Fe content increases and Ni content decreases. As can be seen from Fig. 4, Ni substitution at the A site contributes more than Fe to enhance the M_s in the Co-dominant spinel structure, which could be attributed to stronger superexchange interactions with Co at the B site.[37] Therefore, the higher Ni content in FNC (a) yields higher M_s than that of FNC (b). In addition, synergistic interactions among Ni, Fe, and Co in the ternary metallic FNC (a) spinel contribute to higher M_s than binary metallic $Ni_xCo_{3-x}O_4$ spinel. Some research has also explored the effects of ordered and disordered assembly of magnetic dipoles.[38-40] Here, this spinel material is composed of many small dots, and can be considered as an assembly of nanoparticles, each of which is an independent magnetic dipole. To change the structure and flexibility of these assemblies, we annealed FNC spinel (a) and (b) in an Ar atmosphere at 300°C for 2 hours. The annealed FNC (a) and (b) in Figure 5 show decreased saturation magnetizations of 43.6 emu/g and 30.1 emu/g, which are less than half the values of the original samples. Untreated samples contain intact 3D flower structures with 1D arms, allowing the flexible movement. As mentioned in the mechanism part, these flowers are composed of numerous small spherical dots. The decreased saturation magnetization after annealing suggests that in the flexible structure before annealing some structural ordering can occur upon application of a magnetic field. However, annealing collapsed the flower structure and partially sintered the arms, reducing the flexibility and mobility of arms, and therefore reduced the possibility of structural changes upon application of a magnetic field. In addition, we measured the density of the original and annealed FNC (a) and (b) samples. This aids in explaining why the FNC spinel (a) exhibits higher saturation magnetization than (b). FNC (a) and (b) show similar density (Table S1) of 3.67 g/cm^3 and 3.91 g/cm^3, increasing to 5.47 and 5.22 g/cm^3 after annealing, respectively. From the TEM images (Figure 5), overall particle size decreased a bit after annealing. Heating at 300°C can only remove the surfactants promote the close packing of nanoparticles. In the meanwhile, the flower structures partially collapse, aggregating the arms to the cores and the cores shrink in size, resulting a higher density and lower ability to reorder. Moreover, the BET results show a decreased specific surface area (Table S2) from the original M-SCO samples (50.9 m^2/g) to those annealed at 300 °C (36.1 m^2/g), consistent with collapse of the arms of the structures. Both density and SSA results support that annealing increased the density and reduced the flexibility of the flower-like structures, which constrained the ordering of the anisotropic crystal structure in a magnetic field and decreased the saturation magnetization.

Comparing FNC (a) and (b), FNC (a) with higher Ni content and lower Fe content exhibited higher saturation magnetization. This is consistent with the results in Figure 4 showing that Ni-SCO had higher saturation magnetization than Fe-SCO.

However, FNC (b) with more Fe produced a larger core structure, and thus less flexible magnetic domains. In Table S4, we compared the saturation magnetization of cobalt spinel materials with different compositions synthesized via vapor-, solution-, and solid-phase methods in recent years. The saturation magnetization is reported in each of these studies, in all cases showing lower M_s than our best FNC spinel sample. Others' observations of reduced M_s upon doping Mn in the cobalt spinel structure are consistent with our results presented above.

In sum, the saturation magnetization varies strongly with the composition of these spinel materials, among which we find a ternary FNC spinel with a saturation magnetization of 98.6 emu/g, which to the best of our knowledge exceeds that of previously reported spinel nanostructures. Also, by comparing annealed and untreated samples, we explored the effect of magnetic order on saturation, proving that the flexibility of this hierarchical crystal structure plays an essential role in enhancing the saturation.

3. Conclusion

We synthesized a flower-like hierarchical spinel type cobalt oxide, which can serves as a general structural template to produce other $M_xCo_{3-x}O_4$ spinels (M = metal element) with the same flower-like morphology. The SCO template, Fe-SCO, Mn-SCO, and Ni-SCO were selected as representative examples to explore the optimal conditions to synthesize the hierarchical flower-like structures and probe the mechanisms of their formation. All the reaction parameters such as the amounts of ligands and additives, heating rates, and duration were studied to explore morphology evolution, providing rational guidance for the future synthesis of M-SCOs.

Different growth mechanisms of Fe-SCO and other M-SCOs were revealed by combining studies of morphology evolution and the composition, demonstrating that the morphology and magnetic properties can be tuned by controlling the composition of samples.

All these M-SCOs are ferromagnetic due to the SCO template crystal structure. We measured magnetization curves for the SCO template, Fe-SCO, Mn-SCO and Ni-SCO representatives, which led us to synthesize a ternary FNC spinel containing Fe, Ni, and Co. This spinel exhibited a saturation magnetization higher than any previous reports for such spinel oxide nanostructures.

We summarized 23 types of M-SCOs that has been synthesized so far, illustrating the stability and extensibility of this flower-like hierarchical SCO template. This study demonstrated a synthesis strategy of a new type of spinel cobalt oxide and developed M-SCO materials. This provides a previously unavailable comprehensive and systematic understanding of these nanomaterials that can provide rational guidance for future exploration. Also, the controlled morphology, magnetic properties, and ability to incorporate numerous dopants that bring their own useful properties provide tremendous potential for this approach across multiple application areas.

4. Experimental

Chemicals. Cobalt (II) acetylacetonate ($Co(acac)_2$) 99%, iron (III) acetylacetonate ($Fe(acac)_3$) 99+%, manganese (III) acetylacetonate ($Mn(acac)_3$) 97% and nickel (II) acetylacetonate ($Ni(acac)_2$) 96% were purchased from Acros Organics. Octadecene (ODE) 90%, benzyl ether (BE) 99%, dodecylamine (DDA) 98%, trioctylphosphine (TOP) 97%, 1,2-dodecanediol (DDD) 90%, 1,2-tetradecanediol (TDD) 90%, oleic acid (OA) 90%, and oleylamine (OAm) 70% were purchased from Sigma Aldrich. Precursors used for synthesizing $M_xCo_{3-x}O_4$ NCs with M = Cu, Ag, Zn, Pd, Mo, Gd, Pt, Al, K, Li, and Cr are listed in the supporting information Excel file.

Characterization. TEM and HRTEM images were acquired using a JEOL 2010 microscope at 107 mA and 200 kV. XRD patterns were collected using a Rigaku Ultima IV with Cu Kα X-ray source. Magnetic properties were tested using the VSM mode of a Quantum Design Physical Property Measurement System (PPMS) model 6000 at 300K. SEM imaging was conducted using a Carl Zeiss Auriga crossbeam focused ion beam scanning electron microscope (FIB-SEM).

Synthesis of SCO and M-SCO. We used a one-step solution phase synthesis method in which precursors ($Co(acac)_2$, $Fe(acac)_3$, $Mn(acac)_3$ and $Ni(acac)_2$), solvents (ODE or BE), ligands (DDD, TDD, or DDA) and additives (OA, OAm, and TOP) were mixed in a three-neck flask at ambient conditions, then heated with stirring to 110 ^oC under flowing Ar for 30 min to remove dissolved oxygen and water from the solution. Then, the flask was wrapped with one piece of glass wool to improve temperature uniformity, and heated to 270 ^oC over a period of 60 min at a constant ramp rate of 2.7 ^oC/min. For M-SCO synthesis, the M to Co metal ratio was 0.5:1 for most experiments, but was reduced to 0.3:1 or 0.1:1 in some cases. The detailed synthesis parameters for each reported sample are tabulated in the supporting information (Table S1).

Conflicts of interest

There are no conflicts to declare.

Acknowledgements

This work was supported in part by NSF grant CBET-1337860, by the RENEW Institute of the University at Buffalo, and by the New York State Center of Excellence in Materials Informatics.

References

1 W. H. Bragg, *Nature*, 1915, **95**, 561.

2 T. Yao, X. Guo, S. Qin, F. Xia, Q. Li, Y. Li, Q. Chen, J. Li and D. He, *Nano-Micro Lett.*, 2017, **9**, 38.

3 J. Deng, L. Kang, G. Bai, Y. Li, P. Li, X. Liu, Y. Yang, F. Gao and W. Liang, *Electrochim. Acta*, 2014, **132**, 127.

4 A. K. Kushwaha, Ş. Uğur, S. Akbudak and G. Uğur, *J. Alloys Compd.*, 2017, 704, 101-108.

5 S. Ouyang, Z. Li, Z. Ouyang, T. Yu, J. Ye and Z. Zou, *J. Phys. Chem. C*, 2008, **112**, 3134.

6 Y. P. Zhu, T. Y. Ma, M. Jaroniec and S. Z. Qiao, *Angew. Chem. Int. Ed. Engl.*, 2017, **56**, 1324.
7 W. Yang, Y. Yu, Y. Tang, K. Li, Z. Zhao, M. Li, G. Yin, H. Li and S. Sun, *Nanoscale*, 2017, **9**, 1022.
8 H. Zhu, S. Zhang, Y.-X. Huang, L. Wu and S. Sun, *Nano Lett.*, 2013, **13**, 2947.
9 L. Wu, P. O. Jubert, D. Berman, W. Imaino, A. Nelson, H. Zhu, S. Zhang and S. Sun, *Nano Lett.*, 2014, **14**, 3395.
10 J. F. Marco, J. R. Gancedo, M. Gracia, J. L. Gautier, E. I. Ríos, H. M. Palmer, C. Greaves and F. J. Berry, *J. Mat. Chem.*, 2001, **11**, 3087.
11 P. Mountapmbeme Kouotou, H. Vieker, Z. Y. Tian, P. H. Tchoua Ngamou, A. El Kasmi, A. Beyer, A. Gölzhäuser and K. Kohse-Höinghaus, *Catal. Sci. Technol.*, 2014, **4**, 3359.
12 P. Nkeng, S. Marlier, J. F. Koenig, P. Chartier, G. Poillerat and J. L. Gautier, *Electrochim. Acta*, 1998, **43**, 893.
13 G. R. Peterson, F. Hung-Low, C. Gumeci, W. P. Bassett, C. Korzeniewski and L. J. Hope-Weeks, *ACS Appl. Mater. Interfaces*, 2014, **6**, 1796.
14 X. Li, L. Yuan, J. Wang, L. Jiang, A. I. Rykov, D. L. Nagy, C. Bogdan, M. A. Ahmed, K. Zhu, G. Sun and W. Yang, *Nanoscale*, 2016, **8**, 2333.
15 H. B. Wu, H. Pang and X. W. Lou, *Energy Environ. Sci.*, 2013, **6**, 3619.
16 T. Maiyalagan, K. A. Jarvis, S. Therese, P. J. Ferreira and A. Manthiram, *Nat. Commun.*, 2014, **5**, 3949.
17 X. Wu and K. Scott, *J. Mater. Chem.*, 2011, **21**,12344.

18 I. Srnová-Šloufová, B. Vlcková, Z. Bastl and T. L. Hasslett, *Langmuir*, 2004, **20**, 3407.
19 U. I. Tromsdorf, N. C. Bigall, M. G. Kaul, O. T. Bruns, M. S. Nikolic, B. Mollwitz, R. A. Sperling, R. Reimer, H. Hohenberg and W. J. Parak, *Nano letters*, 2007, **7**, 2422.

20 S. Sun, H. Zeng, D. B. Robinson, S. Raoux, P. M. Rice, S. X. Wang and G. Li, *J. Am. Chem. Soc.*, 2004, **126**, 273.
21 L. Qiao, Z. Fu, J. Li, J. Ghosen, M. Zeng, J. Stebbins, P. N. Prasad and M. T. Swihart, *ACS Nano*, 2017, **11**, 6370.
22 W. Bu, Z. Chen, F. Chen and J. Shi, *J. Phys. Chem. C*, 2009, **113**, 12176.
23 A. Mendoza-Garcia, H. Zhu, Y. Yu, Q. Li, L. Zhou, D. Su, M. J. Kramer and S. Sun, *Angew. Chem. Int. Ed. Engl.*, 2015, **54**, 9642.
24 Z. Xu, C. Shen, Y. Hou, H. Gao and S. Sun, *Chem. Mater.*, 2009, **21**, 1778.
25 K. A. Abel, J. Shan, J.-C. Boyer, F. Harris and F. C. J. M. van Veggel, *Chem. Mater.*, 2008, **20**, 3794.
26 V. Sharma, C. Chotia, Tarachand, V. Ganesan and G. S. Okram, *Phys. Chem. Chem. Phys.*, 2017, **19**, 14096.
27 M. Oku and K. Hirokawa, *J. Electron Spectrosc. Relat. Phenom.*, 1976, **8**, 475.
28 V. K. LaMer and R. H. Dinegar, *J. Am. Chem. Soc.*, 1950, **72**, 4847.
29 H. Vehkamäki, *Springer Science & Business Media*, 2006.
30 L. Qiao and M. T. Swihart, *Adv. Colloid Interf. Sci.*, 2017, **244**, 199.
31 Z. Xi, J. Li, D. Su, M. Muzzio, C. Yu, Q. Li and S. Sun, *J. Am. Chem. Soc.*, 2017, **139**, 15191.
32 X.-W. Wei, G.-X. Zhu, Y.-J. Liu, Y.-H. Ni, Y. Song and Z. Xu, *Chem. Mater.*, 2008, **20**, 6248.
33 T. Lu le, N. T. Dung, D. Tung le, C. T. Thanh, O. K. Quy, N. V. Chuc, S. Maenosono and N. T. Thanh, *Nanoscale*, 2015, **7**, 19596.
34 S. M. Ansari, B. B. Sinha, D. Phase, D. Sen, P. U. Sastry, Y. D. Kolekar and C. V. Ramana, *ACS Appl. Nano Mater.*, 2019, **2**, 1828.
35 L. Zhang, R. He and H.-C. Gu, *App. Surf. Sci.*, 2006, **253**, 2611.
36 H. Moradmard, S. Farjami Shayesteh, P. Tohidi, Z. Abbas and M. Khaleghi, J. Alloys Compd., 2015, **650**, 116.
37 N. Deraz, *Ceram. Int.,* 2012, **38**, 511.
38 M. Varon, M. Beleggia, T. Kasama, R. J. Harrison, R. E. Dunin-Borkowski, V. F. Puntes and C. Frandsen, Sci Rep, 2013, **3**, 1234.
39 J. Chen, A. Dong, J. Cai, X. Ye, Y. Kang, J. M. Kikkawa and C. B. Murray, *Nano Lett.*, 2010, **10**, 5103.
40 J. M. Luttinger and L. Tisza, *Phys. Rev.*, 1947, **72**, 257.

TOC entry:

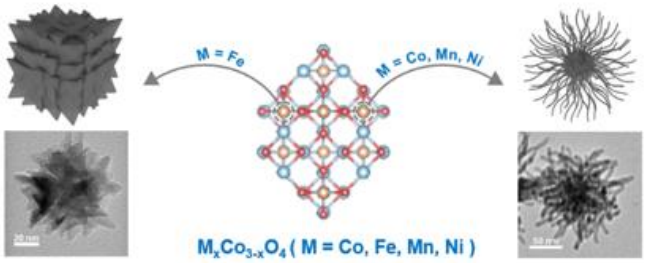

A robust and general method for producing cobaltite spinel nanostructures containing a broad array of additional elements is presented.